Stealth pressurisation of boiling magma limits geodetic detectability of volcanic eruptions

Gregor Weber[a,b], Juliet Biggs[b], Alain Burgisser[c], Catherine Annen[d]

a. *School of Ocean and Earth Science, University of Southampton, Southampton, United Kingdom*.
b. *COMET, School of Earth Sciences, University of Bristol, Bristol, United Kingdom*.
c. *Univ. Grenoble Alpes, Univ. Savoie Mont Blanc, CNRS, IRD, Univ. Gustave Eiffel, ISTerre, 38000, Grenoble, France*.
d. *Institute of Geophysics of the Czech Academy of Sciences, Prague, Czech Republic*.

Corresponding author: Gregor Weber (g.weber@soton.ac.uk)

Abstract

Crystallisation-driven volatile exsolution (second boiling) is widely invoked to pressurise shallow magma reservoirs, yet its ability to generate eruption-triggering overpressure and detectable ground deformation is poorly quantified. We couple phase equilibria with thermal and viscoelastic models of sill-like intrusions to map pressure evolution and geodetic detectability of second boiling. Thermodynamic calculations for basaltic and rhyolitic magmas from Askja (Iceland) and Puyehue-Cordón Caulle (Chile) are embedded in conductive thermal models for thin (20 m) and thick (200 m) sills at 2-4 km depth, and the resulting volume changes and magma compressibility are propagated into pressurisation histories and volume-change rates. Hydrous magmatic sills can develop overpressures of 20-30 MPa on timescales of months to centuries depending on initial sill size and crustal parameters, whereas relatively dry basalt undergoes cyclic behaviour with contraction followed by modest re-pressurisation. For a given composition and depth, thin and thick sills attain similar overpressures but differ by an order of magnitude in volume-change rate. Only small volatile-rich sills exceed geodetic resolution thresholds. In felsic crust, viscoelastic relaxation further dampens surface deformation, consistent with globally observed reduced deformation at arc volcanoes. Applied to Askja, cooling of a basaltic sill can explain the subsidence from 1983-2021, while second boiling in a small rhyolitic body can plausibly contribute to rapid uplift observed starting in mid-2021. Our results define a regime of "stealth" pressurisation in shallow hydrous reservoirs in mafic-intermediate crust, where eruption-scale overpressure can accumulate with undetectable geodetic unrest and help explain unexpected explosive eruptions with little precursory deformation.

Keywords: Magma overpressure; Second boiling; Volcano deformation; Askja caldera; Viscoelastic crust

Highlights

- Assessment of eruption potential and geodetic detectability of second boiling
- Stealth pressurisation by second boiling can explain unexpected eruptions
- Reservoir size, not peak overpressure, mainly controls geodetic detectability
- Felsic arc crust damps deformation, consistent with fewer signals than ocean islands

1. Introduction

Volatile exsolution is fundamental to how magmas pressurise, ascend, and erupt (Edmonds and Wallace, 2017). In upper crustal reservoirs that cool and crystallise at near-constant lithostatic pressure, volatile saturation is often achieved not by decompression (i.e. first boiling), but by crystallisation-driven enrichment of volatiles in the residual melt. This process, commonly termed second boiling, generates a separate fluid phase and can substantially modify both the volume and compressibility of magma. Whether second boiling, by itself, plays a central role in eruption initiation and whether this process produces detectable unrest signals, remains a central question in volcanology.

The idea that crystallisation-driven volatile oversaturation might trigger eruptions has a long history in analytical models of silicic magma chambers. Blake (1984) showed that volatile oversaturation in closed, cooling rhyolitic chambers could, in principle, generate overpressures of several tens of MPa and fracture chamber roofs. Tait et al. (1989) extended this framework, emphasising how gas content and pressure may control eruption periodicity. Tracking these processes in observations has proven more difficult, as the interpretation of volcano monitoring data in terms of the magmatic processes that generate them is often non-unique (Gottsmann et al., 2017; Poland and Anderson, 2020), and volatile oversaturation may leave only sparse evidence in the chemistry and textures of erupted rocks (Kent et al., 2023).

Despite these challenges, a growing body of petrological observations points to an important role of second boiling in the build-up to many volcanic eruptions. Apatite crystals, in particular, have emerged as powerful recorders of magma saturation history, as their F-Cl-OH systematics, combined with thermodynamic partitioning models, allow reconstruction whether melts were volatile-undersaturated or fluid-saturated at the time of apatite growth (Li et al., 2021; Popa et al., 2021; Stonadge et al., 2023). Applications at Campi Flegrei in Italy (Stock et al., 2016), Laacher See in Germany (Humphreys et al., 2021), or Costa Ricas Irazú volcano (Boyce and Hervig, 2009), suggest that explosive eruptions can be preceded by prolonged undersaturation followed by a short-lived episode of volatile saturation and fluid accumulation before eruption. Complementary constraints from melt inclusions, mineral chemistry, and experimental petrology for monitored events such as the 2015 eruption of Calbuco in Chile and the 2014 eruption of Kelud in Indonesia likewise point to the build-up of an overpressured magmatic fluid phase in shallow, long-lived reservoirs that exhibited only limited precursory surface deformation and seismicity (Arzilli et al., 2019; Cassidy et al., 2019; Namur et al., 2020). Although these records make a compelling case that volatile accumulation is a common ingredient in eruption runup and has potential links to the detectability of precursory warning signals, on their own, petrological studies do not quantify

whether second boiling has generated sufficient overpressure to initiate the eruption nor if the process could be detectable in monitoring data. Addressing these problems requires modelling approaches that couple thermodynamic and thermo-mechanical processes.

A wide range of numerical models have explored how volatile exsolution and crustal processes interact to control pressure evolution and deformation in shallow magma reservoirs, indicating that the timing and magnitude of gas-driven pressurisation are sensitive to initial volatile content and composition, magma compressibility, reservoir parameters such as depth and geometry and host-rock rheology (Annen and Burgisser, 2021; Brookfield et al., 2023; Caricchi et al., 2014; Scholz et al., 2023; Spang et al., 2022; Townsend, 2022). Thermal models of incrementally emplaced sills and plutons show that cooling histories depend strongly on intrusion geometry, emplacement style and history (Annen, 2009; Weber et al., 2025), which matters because second boiling is intrinsically cooling-driven. As illustrated in Fig. 1, conductive cooling of a sill-like reservoir produces spatial temperature gradients such that hotter, melt-rich regions may remain volatile-undersaturated while cooler, more crystalline margins cross the saturation boundary and exsolve a fluid phase. Net overpressure reflects then the balance between expansion where second boiling occurs and contraction elsewhere, while the cooling rate and evolving magma compressibility controls the rate of volume change and thus its potential geodetic detectability. The combined influence of this spatially variable temperature structure, saturation state and temperature-dependent crustal rheology on both eruption-triggering overpressure and its surface expression in laterally extensive shallow intrusions, however, remains not well understood but important to link petrological records to monitoring signals, and assess the eruption potential and detectability of second-boiling driven magma pressurisation.

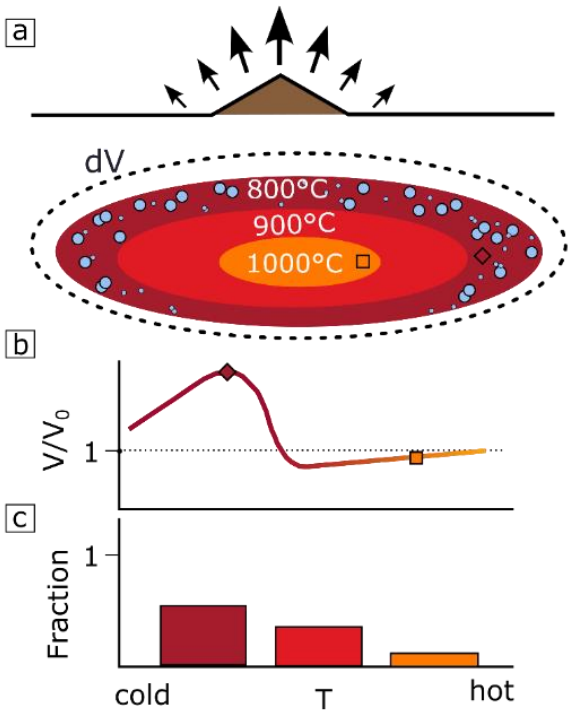

Fig. 1. *Conceptual model linking thermal structure, second boiling, and volume change. A) 2D cross-section of a cooling magmatic intrusion, with colours indication thermal structure. B) Fractional volume change (V/V0) parameterized as function of temperature; different parts of the intrusion are either contracting (orange square) or expanding (red diamond). C) The proportion of magma in each temperature increment governs the volume and pressure evolution during second boiling.*

Here we address this gap by building on and expanding our previous modelling framework (Annen and Burgisser, 2021; Brookfield et al., 2023; Weber et al., 2025). We couple composition-specific phase equilibria with 2.5D axisymmetric heat transfer models and viscoelastic relaxation of the host crust, to map the conditions under which second boiling can generate significant overpressure in shallow crustal intrusions and to assess when the associated volume changes would be detected with current geodetic methods. Our study aims to bridge petrological constraints on magma composition and volatile saturation with the thermo-mechanical response of crustal magma reservoirs and their geodetic expression.

2. Methodology

We simulated the evolution of volume change and pressurisation in magmatic sills undergoing cooling, crystallisation-driven volatile exsolution, and a viscoelastic response of the host rocks. Thermodynamic phase equilibria modelling was used to parameterise how the system volume changed during phase transitions as a function of temperature, while tracking concurrent changes in magma compressibility. The phase equilibria results were then embedded in thermal models and scaled to intrusion size, from which we calculated the intrusion's volume change, pressure evolution, and viscoelastic relaxation history.

2.1. Thermodynamic Modelling

To compute temperature-dependent crystallinity, volatile exsolution, magma compressibility, and resulting system volume changes, we use thermodynamic modelling software rhyolite-MELTS version 1.1 (Gualda et al., 2012). Closed system, isobaric equilibrium crystallisation models from liquidus to near-solidus conditions were run on basalt and rhyolite bulk composition from Askja in Iceland (samples: s_IA1904 and s_ID2403 of Kuritani et al. (2011)) and Puyehue-Cordon Caulle in Southern Chile (samples: s_13822 of Turner et al. (2016), and s_PUY12_BLOCK of Schipper et al. (2015)). These endmembers were chosen because 1) they represent contrasting continental arc and rift/oceanic settings, 2) span a wide range of crystallisation behaviour with regards to melt fraction-temperature relations, and 3) their eruptive products typically do not contain hydrous mineral phases (e.g. amphiboles) that are poorly handled by MELTS. Simulation conditions were informed by published melt inclusion entrapment conditions (Hauri et al., 2017; Schattel et al., 2014), deformation source modelling (Koymans et al., 2023), and experimental petrology (Castro et al., 2013) as listed in supplementary table 1.

Askja Rhyolite simulations were run at 60 MPa, with initial H_2O of 2.7 wt.%, no CO_2, a fixed oxygen fugacity (fO_2) one log unit above the fayalite-magnitude-quartz buffer reaction (FMQ+1), and temperatures between 990-750 °C. For Askja basalt, published volatile data are lacking, so we adopted a pressure of 60 MPa, initial H_2O content of 0.8 wt.% and CO_2 contents of 0.1 wt.%, and fixed oxygen fugacity at FMQ+1. These pressures were also chosen to test whether second boiling could contribute to the observed geodetic unrest at Askja, where source depth of 2-3 km have been inferred (Koymans et al., 2023).

For Puyehue Cordón-Caulle (Puyehue hereafter), pre-eruptive volatile data are lacking, and pressure estimates are limited to water saturated experimental estimates for the 2011 rhyolites (50-100 MPa) (Castro et al., 2013), so we explored generic arc-magma scenarios. Simulations for

both basaltic and rhyolitic compositions were run at 100 MPa, with generic initial H_2O of 4 wt.%, CO_2 of 0.05 wt.%, and fO_2 buffered at nickel-nickel-oxide (NNO).

2.2 Heat Transfer Simulations

To scale the rhyolite-MELTS output to volumetric intrusions, we carried out heat transfer simulations. All simulations were run with a 2.5-dimensional axisymmetric geometry (Fig. 2), in which a magmatic sill (cylindrical sheet) was instantaneously emplaced at its liquidus temperature and cooled until all magma was fully solidified. For each composition, we simulated two geometries: (1) a sill of 200 m thickness (initial volume: 1.41 km^3), and 2) a sill of 20 m thickness (initial volume: 0.14 km^3), both with radius of 1.5 km, in accordance with the natural scaling of sheet intrusion dimensions based on field observations (Cruden et al., 2018). The physical domain was sill-centred and measured 2400 × 1200 m for the thick sill and 2400 × 400 m for the thin sill. Sills were intruded instantaneously at a depth corresponding to the pressure used in the rhyolite-MELTS simulations, assuming an average crustal density of 2700 kg m^{-3}. To bracket endmember behaviour, we ran two scenarios based for each composition/volcano and sill thickness: (a) a fast-cooling scenarios with a geothermal gradient of 30°C km^{-1} and high magma and country rock thermal conductivity of 4.5 W m^{-1} K^{-1}, and (b) a slow-cooling case with geotherm of 90°C km^{-1} and conductivity of 2.5 W m^{-1} K^{-1}. Each volcano/composition scenario is run at a particular depth and initial temperature as specified in section 2.1. Therefore, the thermal conductivity and initial geothermal gradient control the cooling behaviour of the modelled intrusions.

The models were run using the thermal code developed by Weber et al. (2020), which uses conductive heat transfer to simulate magma cooling and evolution. The temporal evolution of temperature in the crust is governed by

$$\rho\left(c_p + L\,\frac{\partial\varphi}{\partial T}\right)\frac{\partial T}{\partial t} = \frac{1}{r}\frac{\partial}{\partial r}\left(kr\frac{\partial T}{\partial r}\right) + \frac{\partial}{\partial z}\left(k\frac{\partial T}{\partial z}\right), \quad (1)$$

where ρ is the density, T is the temperature, t is the time, r is the radial coordinate relative to the axis of symmetry, z is the depth, k is the thermal conductivity, L is the latent heat of crystallization, c is the specific heat capacity, and φ is the melt fraction. Supplementary table 2 summarises the numerical and physical modelling variables for each simulation. Melt fraction was interpolated from rhyolite MELTS output as a smooth, monotonic function of temperature using a shape-preserving cubic spline. Latent heat release was implemented with a non-linear iteration loop because $\partial\varphi/\partial T$ depends on temperature, so the effective heat capacity had to be updated consistently with the evolving T field within each time step. Eq. 1 was solved using a fully

explicit finite difference scheme. Numerical grids of 400 x 200 and 400 x 600 cells were used for 200 m and 20 m thick sill geometries, respectively. The top boundary of the model was a fixed temperature of 10°C and the bottom boundary was fixed at the temperature of the imposed geotherm, and lateral boundaries had zero heat flux. In each cell containing magma above solidus, we tracked the temperature, crystallinity, magma compressibility, and phase change related volume with time. An executable version of the *Matlab* code is available in the supplementary materials.

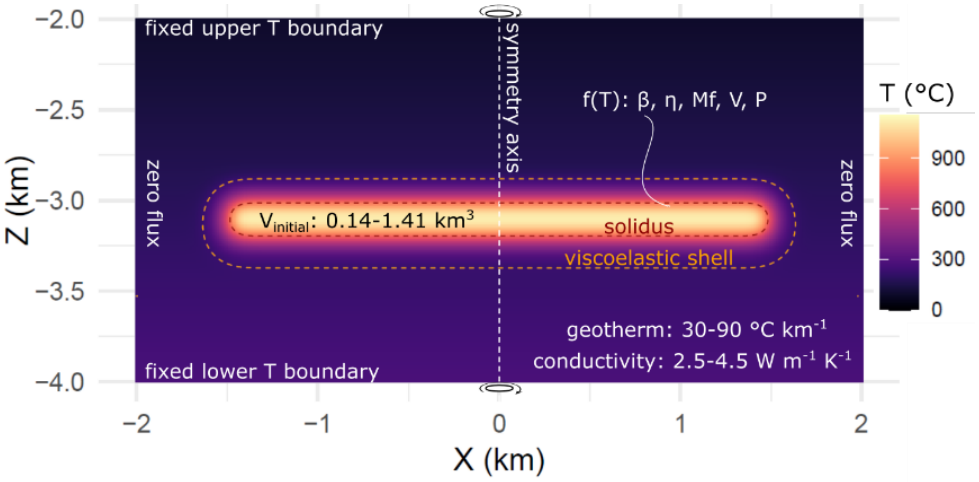

Fig. 2. *Illustration of the axisymmetric 2.5D thermal modelling geometry. A sill of initial volume (0.14 and 1.41 km³) is emplaced at its liquidus temperature and parametrised during cooling for changes in compressibility and volume.*

2.3. Pressure evolution

To calculate the pressurisation history of the simulated magmatic sills, we tracked the difference between the volume of the magmatic sill ($V_{cooling}$) above solidus (only considering volume change in response to cooling but no expansion/contraction) and the system volume change (V_{sys}) resulting from phase changes such as crystallisation (contraction) and volatile exsolution (expansion) at each timestep. Although both V_{sys} and $V_{cooling}$ were smooth curves with respect to time, the resulting difference ($\Delta V_{sys}(t)$) showed steps and oscillations resulting from numerical discretization. To resolve this, we used Savitzky-Golay smoothing, which fits a low degree polynomial in a moving window, preserving peaks and timing while not shifting features in time (Fig. SM1).

The pressure calculations combined the relationship of volume changes and magma compressibility in a magma reservoir system (Kilbride et al., 2016; Rivalta and Segall, 2008; Yip et al., 2022). The normalised subsurface volume change of a reservoir (V_c) is written as

$$V_c = \Delta V_{sys} \left(1 + \frac{\beta_m}{\beta_c}\right)^{-1}, \quad (2)$$

where ΔV_{sys} is the volume change resulting from phase transitions, β_m is the magma compressibility and β_c is the compressibility of the chamber geometry.

Using the definition of the isothermal compressibility, $\beta = (1/V)(\Delta V/\Delta P)$, the pressure change associated with a source volume ΔV_{sys} change embedded in a reservoir of the volume V_c is

$$\Delta P(t) = \frac{\Delta V_{sys}}{V_c(\beta_m + \beta_c)} \quad (3)$$

We compute $\Delta V_{sys}(t)$ from the thermodynamic model as the time-dependent magma volume change and express it as a fractional volume change

$$fV(t) = \frac{\Delta V_{sys}}{V_c} \quad (4)$$

Scaling the phase change volume by the thermal volume of the intrusion and substituting $V_{sys}(t) = fV(t)\ V_c$ into the expression above yields

$$\Delta P(t) = \frac{fV(t)}{\beta_m + \beta_c} = \frac{fV(t)}{\beta_{eff}} \quad (5)$$

where β_{eff} is the sum of the compressibility of the magma (β_m) and chamber geometry (β_c). The latter was calculated based on analytical solutions for an elliptical geometry and the considered sill dimensions (Rivalta and Segall, 2008; Yip et al., 2022).

2.4. Viscoelastic relaxation

We started from a purely elastic pressurisation history derived from the volume-pressure relation and allowed this overpressure to relax through time as the surrounding crust behaved viscoelastically. In contrast to previous work (Brookfield et al., 2023), we treated the wall rocks as a Maxwell material whose relaxation time (τ) varied in time according to the evolving temperature field.

The temperature field above the centre of the intrusion was tracked in time, so that only elements that were hotter than 500 K contributed to viscoelastic relaxation. Cooler elements were treated

as purely elastic and excluded from the calculations. The viscosity of crustal rocks was calculated using an Arrhenius law (e.g. Head et al., 2021) of the form

$$\eta(x,z,t) = A_d \exp\left(\frac{A_e}{R(T(x,z,t)-273.15)}\right), \quad (6)$$

Where A_d is the pre-exponential Dorn factor, A_e is an activation energy parameter, and R is the gas constant. We systematically varied the parameters between A_e=5×10^9-2×10^{13} Pas and A_d=106-219 kJ/mol, in accordance with available experimental data (Kirby and Kronenberg, 1987; Morales Rivera et al., 2019; Ranalli and Murphy, 1987).

Because viscosity follows an Arrhenius law, temperature variation in the hot shell surrounding the intrusion leads to exponential variation in the viscosity of the crustal rocks surrounding the intrusion. We approximate the effective viscosity of the crust as a single time-dependent value in order to define the Maxwell relaxation time. At each timestep, we computed a spatially averaged effective viscosity by taking the geometric mean over all active elements (T>500 K). We then calculated the corresponding Maxwell relaxation time as

$$\tau(t) = \frac{\eta_{gm}(t)}{G}, \quad (7)$$

where the shear modulus G was 40 GPa. In a Maxwell material held at an initial stress σ_0, stress relaxes as $\sigma(t) = \sigma_0\, e^{-t/\tau}$. We used the same principle for overpressure relaxation. The viscous contribution from previous timesteps, D_{i-1}, decays over a time step Δt_i as $D_{i-1}\, e^{-\Delta ti/\tau i}$, which gives the exponential factor in our update. During the same interval, the current elastic overpressure generates additional relaxation, approximated by a first-order term, so that

$$D_i = D_{i-1} \exp\left(-\frac{\Delta t_i}{\tau_i}\right) + \frac{P_{input,i}}{\tau_i}\, \Delta t_i \quad (8)$$

The surviving overpressure is then

$$P_{relax,i} = P_{input,i} - D_i \quad (9)$$

which is the imposed elastic overpressure (P_{input}) minus the contribution from viscous relaxation. All pressure and viscoelastic relaxation calculations were implemented in *R*. The *R* script is available in the supplementary materials.

3. Results

3.1. Thermodynamic controls on melt fraction, compressibility and system volume

Phase-equilibria calculations show that the temperature interval over which crystals, melt and exsolved fluid coexist, and the magnitude of associated volume changes, differ markedly among the four magmas (Fig. 3). The liquid lines of descent (Fig. 3a) span a similar range in SiO_2 for the two basalts and rhyolites, respectively, but the slope of SiO_2-T and the position of the rhyolite and basalt liquidus differ, reflecting contrasting crystallisation sequences and water contents. The melt-fraction temperature relations (Fig. 3b) define distinct mush windows. Askja and Puyehue basalts exhibit broad, gently curving decreases in melt fraction (φ) from liquidus to solidus, with φ decreasing from ~1 to <0.1 over several hundred degrees. In contrast, both rhyolites crystallise over much narrower temperature ranges. Askja rhyolite remains almost entirely molten at temperatures >900-950°C, but melt fraction drops steeply from φ<0.2 over a <100°C interval near 800-850°C. Puyehue rhyolite has an even narrower, near-eutectic, crystallisation interval, with melt fraction collapsing to near solidus over only a few tens of degrees. These differences suggest that second boiling affects each composition at different melt fractions and over different durations.

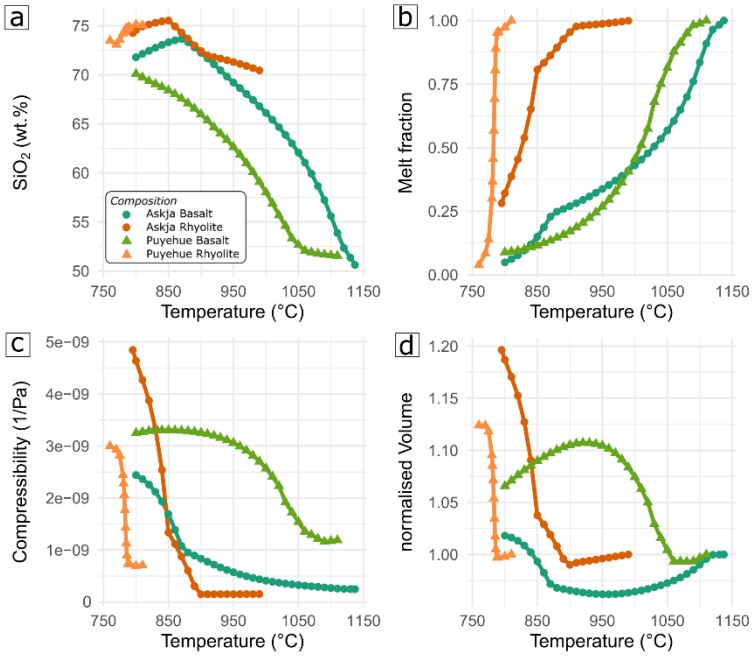

Fig. 3. *Results of thermodynamic (MELTS) simulations for basalt and rhyolite equilibrium crystallisation. Askja basalt is shown as dark green circles and Askja rhyolite as dark orange circles. Puyehue Cordón Caulle is shown as green triangles (basalt) and orange triangles (rhyolite). a) Temperature versus SiO_2 (wt.%) of the melt. b) Melt fraction-temperature relations. c) Magma compressibility (β_m) evolution, and d) Normalised magma volume with temperature.*

Second boiling is clearly expressed in the temperature dependence of magma compressibility (Fig. 3c). Compressibility is relatively low and nearly monotonic in the hot, crystal-poor regime, but increases sharply once volatile saturation is reached. Hydrous compositions show the largest peaks: Puyehue basalt and both rhyolites attain peak compressibilities of order 3-5×10^{-9} Pa^{-1} at melt fractions of ~0.2-0.6. In contrast, the drier Askja basalt displays a more muted and broader compressibility increase that never exceeds ~2-3×10^{-9} Pa^{-1}. Thus, for hydrous magmas, second boiling not only produces a gas phase but also increases the compressibility of the remaining magma.

The net system volume change (melt + crystals + fluid) during magma crystallisation shows a non-monotonic evolution (Fig. 3d). All four compositions undergo overall contraction of a few percent during initial cooling, as crystal formation densifies the systems. For the relatively dry Askja basalt, this episode starts at about 860°C, upon which volatiles saturate, and the system expands. The hydrous compositions show peak expansion of 11 to 20% relative to the liquidus intrusion volume, with the rate of volume change depending on the liquid line of descent (c.f. Fig. 3b). Even though compressibility peaks over the same temperature range, second boiling drives large volume increases.

Taken together, the results show that second boiling primarily redistributes volume change in temperature and greatly increases magma compressibility over a temperature window that depends on the volatile saturation conditions and magma composition. Whether this leads to net pressurisation therefore depends on the cooling history and thermal structure of the reservoir.

3.2. Cooling timescales and magma volume evolution

Cooling rates impact the rates of volumes change with bearing on detectability and pressurisation. We therefore embedded the MELTS-derived functions in conductive cooling models of sills to determine how magma volumes change as intrusions cool (Fig. 4). Sill thickness (H) exerts the strongest control on timescales. For 200 m thick sills (initial volume 1.41 km^3), total magma volume decreases quasi-exponentially, typically over ~200-500 years (Fig. 4a-d), while 20 m thick sills (0.14 km^3) solidify within ~2-5 years (Fig. 4e-f). This scaling is consistent with the expected diffusion timescale $\propto H^2/k$.

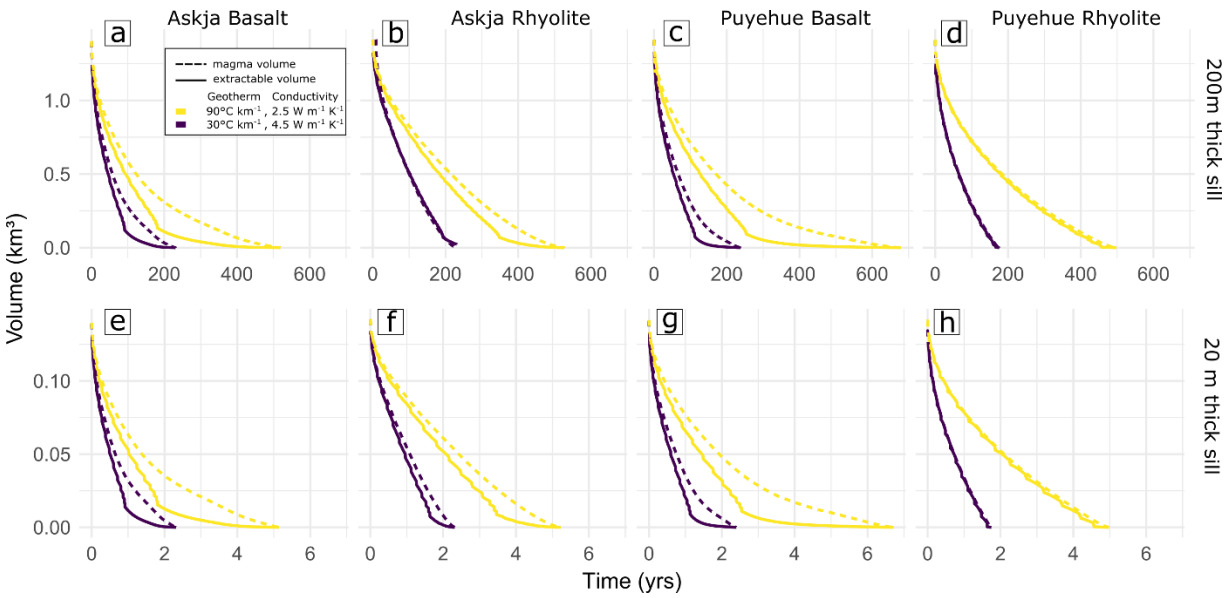

Fig. 4. *Volume evolution of cooling magmatic intrusions over time. Dashed lines show evolving magma volumes and solid lines the extractable magma volume (>50% melt fraction and interstitial melt). a-d) Results for the large sill geometry (200 m thickness), and e-h) results for the small geometry (20m).*

The background thermal structure of the crust modulates these timescales. In the "cold, conductive" endmember (30°C km^{-1} geotherm, k = 4.5 W m^{-1} K^{-1}, purple curves), intrusions cool more quickly by a factor of 2 to 3 compared to the "hot, less conductive" endmember (90°C km^{-1} geotherm, k = 2.5 W m^{-1} K^{-1}, yellow curves). The volume of magma that is potentially eruptible was quantified by calculating a weighted average extractable magma volume by considering all magma above the rheological locking point at a melt fraction of 0.5 and all interstitial melt that can be potentially extracted following the method as laid out by (Weber et al., 2020). In the basaltic cases, extractable magma volumes closely follow the total volume evolution during the initial stages of cooling but diverge to smaller fractions once the magma above the rheological locking point gets exhausted. In contrast, for the rhyolite cases most of the volume remains extractable during crystallisation, in particular for the near eutectic Puyehue scenario with a steep crystallisation curve.

Despite difference in the liquidus-solidus intervals, composition has a secondary although noticeable effect on the cooling behaviour. Puyehue basalt crystallises over a slightly longer timescale than Askja basalt (~700 years for the thick sill; ~7 years for the thin sill), consistent with its broader, more non-linear melt fraction temperature path and associated latent heat release, which keeps the sill centre above the solidus for longer.

3.3. Pressurisation histories, geodetic signatures, and viscoelastic relaxation

Combining the temperature-dependent volume change histories with the corresponding compressibility evolution, we obtained pressurisation histories of the magmatic sills (Fig. 5). Two endmember behaviours emerge: (i) a strongly under-pressured phase followed by modest re-pressurisation for the relatively dry Askja basalt, and (ii) largely monotonic pressurisation up to a peak value followed by a trend towards lower pressures for the more hydrous scenarios.

In the Askja basalt models (Fig. 5a, e) rapid cooling and crystallisation initially dominate over volatile exsolution, causing the sill to contract and develop substantial underpressure. Pressure change drop by about -25 to -35 MPa within one to two years (thin sill) and 100 to 200 years for the thick sill, depending on crustal properties. As the systems cools further, the increasing fraction of magma undergoing second boiling offsets this contraction, so that pressures recover towards, and eventually exceed, the initial lithostatic value. Final overpressures in these runs are nevertheless modest, reaching only a few MPa above the initial state.

By contrast, the Askja rhyolite and both Puyehue compositions (Fig. 5b-d,f-h) are pressurised almost from the outset, as the fraction of boiling magma increases rapidly. For these more hydrous magmas, volatile exsolution is sufficient to compensate contraction due to crystallisation so pressure changes increase from lithostatic to magmastatic peak values on the order of 20-30 MPa without passing through the underpressured stage. After reaching their maximum, overpressures decline slightly due to the increasing amount of magma at temperatures corresponding to lower system volume changes.

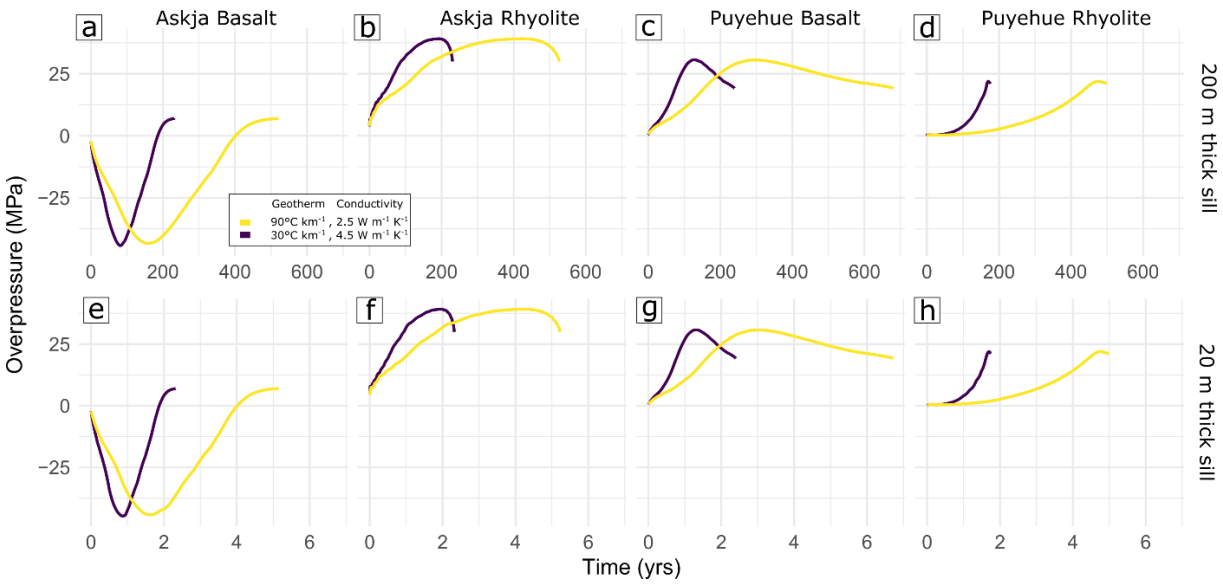

Fig. 5. Pressures evolution of magmatic sills over time. Yellow lines show the slow-cooling and purple lines the fast-cooling scenarios. a-d) Results for the large sill geometry (200 m thickness), and e-h) small geometry (20m).

Sill thickness primarily rescales the timescale over which these pressure changes occur. Thin sills reach their peak overpressures within one to two years and thick sills within 100 to 200 years in all hydrous scenarios. For a given composition and crustal structure, however, the magnitude of the peak overpressure is similar for both sill sizes, indicating that the thermodynamic properties of the magma and the host rheology, rather than the geometry, set the maximum ΔP. Host-rock thermal structure mainly shifts the timing of pressurisation. In the hotter, low conductivity crust, sills reach peak overpressure later than in the colder, more conductive crust. As increasing pressure increases volatile solubility (Shishkina et al., 2010), we carried out mass balance and solubility calculations to quantify the impact of this feedback mechanisms and find that the pressure increase would only result in gas fraction changes typically less than 10%, as shown in supplementary Fig. 2. Bubble resorption is therefore unlikely to significantly reduce overpressures from second boiling.

To connect the eruption initiation potential (overpressure) to geodetic observations, we recast the results in term of the volume change rate (dV/dt, Fig. 6), which is a key parameter that can be obtained from inversion of surface deformation data. Note that the rate of volume change is calculated from the system volume change in response to phase changes (i.e. V_{sys} in Eq. (2)) and not from the cooling volume change shown in Fig. 4. In all cases, the large sills evolve at low volumetric change rates (± 0.0005 km^3 yr^{-1}), consistent with slow cooling. For reference, a deformation rate that typically can be reliably detected with state-of-the-art methods of ~1 cm/yr

surface corresponds to dV/dt = 0.0005-0.001 $km^3\ yr^{-1}$ for a 3.5-5 km deep Mogi source. In contrast, small sills change volume much more rapidly, producing dV/dt of up to 0.005 $km^3\ yr^{-1}$. These high rates still produce large absolute values of vertical displacement (3–6 cm of uplift for a small sill at 3.5-5 km depth inflating at 0.003 $km^3\ yr^{-1}$ for 1 yr). Thus, while all hydrous scenarios undergoing second boiling evolve towards overpressures that are well beyond typical thresholds considered to be sufficient to initiate eruptions (i.e. 10 MPa in shallow crustal environments), only small, volatile-rich sills can generate rates of volume change that are within current geodetic resolution limits.

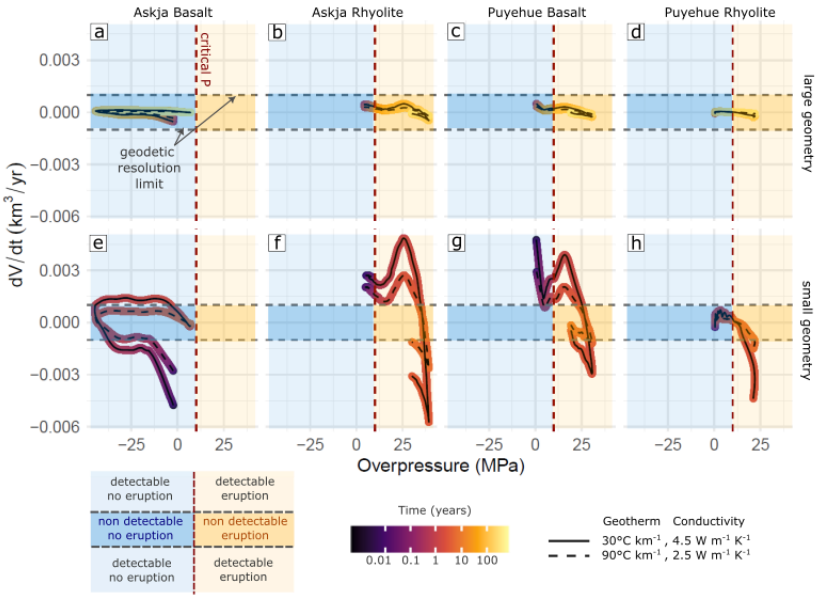

Fig. 6. *Plots showing the geodetic detectability expressed as rate of volume change (dV/dt) versus eruption triggering potential as quantified by overpressure. Colour coding of the fields indicates eruption potential based on an overpressure of 10 MPa (red dashed line) and geodetic detectability based on typical thresholds of 0.001 km^3/yr. The small intrusions are typically within the detectability window while larger sills are below the thresholds. Colour coding of lines reflects time in years, solid and dashed lines represent the fast and slow cooling scenarios, respectively.*

Our thermo-viscoelastic models show that relaxation of intrusion overpressure is highly sensitive to the rheology, and hence composition, of the surrounding crust. Even for an initially cold, shallow crust, magmatic heating combined with a felsic Arrhenius flow law produces low effective viscosities above the viscoelastic threshold and Maxwell relaxation times that are short compared to cooling timescales, such that overpressures generated during sill cooling are rapidly dissipated. In our increasingly felsic scenarios (Fig. 7a,b; Ad= 5.0×10^9 Pas, Ae=106 kJ mol^{-1}), this

manifests as strongly muted net overpressure evolution for both small and large sills, whereas the intermediate-crust parameter set (Ad=3.03×10^{11} Pas, Ae 219 kJ mol^{-1}) yields viscosity high enough that the Maxwell timescales far exceed the cooling duration, leading to a quasi-elastic response in which overpressure cannot be significantly relaxed.

4. Discussion

4.1. Stealth pressurisation and unexpected eruption risk

Our models show that second boiling of hydrous magmas in mafic to intermediate crust can drive shallow intrusions to eruption-scale overpressures while producing deformation rates that are, in many cases, effectively invisible to current geodetic networks. For a given composition and depth, both the thin (H=20 m; V=0.14 km^3) and thick (H=200 m; V=1.4 km^3) sill scenarios can reach comparable maximum overpressures (tens of MPa), but the associated volume change rates differ by more than an order of magnitude (Fig. 5, 6, 7). Thin sills pass through phases where $|dV/dt|$ is on the order of 10^{-3} km^3 yr^{-1}, whereas thick sills evolve at $|dV/dt|$ generally well below this value (IQR: ~10^{-4}; median: ~10^{-6} km^3 yr^{-1}). For a shallow source at 3-5 km depth, a rate of 10^{-3} km^3 yr^{-1} corresponds to a central uplift of roughly 1-4 cm yr^{-1} in a simple Mogi model, while rates an order of magnitude smaller produce sub-centimetre-per year signals. These values are comparable to practical InSAR detection thresholds of ~0.5-3 cm yr^{-1} inferred from regional and global volcanic time-series (Albino et al., 2022; Biggs et al., 2022; Ebmeier et al., 2018). In other words, in our thick-sill scenarios the magnitude of overpressure is not the limiting factor for detectability. It is the small, slowly varying $|dV/dt|$ that allows crystallisation-driven pressurisation to proceed “stealthily” beneath the resolution of present-day monitoring. This behaviour is consistent with the modelling results of Townsend (2022), who showed that second boiling-driven deformation in thermally mature crust should rarely exceed ~1 mm yr^{-1}. Our simulations extend this conclusion by demonstrating that deformation rates remain low even for purely elastic crust, and that intrusion size is a first-order control on detectability.

This stealth pressurisation mechanism is consistent with a growing class of eruptions that show clear evidence for shallow, volatile-rich magma but little precursory warning. At Kelud (2014), experimental phase equilibria and melt inclusions indicate storage of basaltic andesite at ~2-4 km depth under relatively cool, water saturated conditions, and petrological studies argue that fluid exsolution and accumulation in the reservoir play a key role in triggering short-lived explosive eruptions with brief unrest (Cassidy et al., 2019; Utami et al., 2021). The 2015 sub-Plinian eruption of Calbuco likewise tapped a shallow, crystal-rich andesitic magma in the upper crust, with

volatile accumulation in the shallowest storage region invoked as a key factor in this unexpected explosive eruption (Arzilli et al., 2019; Namur et al., 2020). Similar behaviour is documented in the Aleutian Arc (e.g. Mount Veniaminof (Li et al., 2025), Cleveland volcano (Iezzi et al., 2020)). At Mount Veniaminof, most eruptions since the 1990s have not shown clear precursory unrest in either seismic or geodetic data (Cameron et al., 2018). Using numerical modelling, Li et al. (2025) attribute this behaviour to a low magma flux into a small to moderate size reservoir (~0.8-5 km^3) in hot, weak crust, which effectively dampens deformation. Our results are conceptually consistent with their conclusion that reservoir configuration and host-rock rheology largely control whether unrest is observable, but they emphasis a different trigger. Even in the absence of recharge, second boiling in shallow, hydrous intrusions can build eruption-scale overpressure while keeping deformation below detection limits, offering an internally grounded route to stealthy eruption triggering.

A key temporal implication of our results is that, because large shallow sills cool on centennial timescales, intrusions emplaced well before modern monitoring began may still be undergoing stealth pressurisation today. This risk is particularly severe for shallow silicic bodies in basaltic crust with near-eutectic crystallisation behaviour. Our models show that because these systems remain melt-rich by forming only a thin mush layer until late in their crystallisation history, they can sustain large eruptible magma fraction at the point where second boiling has already generated substantial overpressure (Figs. 4b,d; 5b,d). Field, drilling and geophysical observations increasingly indicate that shallow silicic magma bodies at depth comparable to our modelled intrusions (~2-4 km) are common in active volcanic regions (Castro et al., 2016; Mattsson et al., 2018; Rooyakkers et al., 2021). For example, the unintentional encounters with silicic magma during geothermal drilling at Kilauea (Teplow, 2009), Menengai (Mbia, 2014), and Krafla (Elders et al., 2014) show that evolved melts can reside as thin lenses in the upper crust without leaving clear geophysical signatures. Rooyakkers et al. (2021) argue that such hidden silicic magma bodies, typically smaller than 1 km^3, may be widespread and can be mobilised with little warning. Our results provide quantitative constraints on the timescales and conditions under which this mobilisation can take place, reinforcing the notion that such systems pose a significant eruption risk.

4.2. Historic unrest at Askja caldera

The long historic record of surface deformation and bimodal eruptive behaviour makes the Askja caldera in Iceland an ideal test case for our second-boiling scenarios. In its recent history the volcano has produced both basaltic and rhyolitic eruptions. Most recently, in 1961 a basaltic fissure opened, producing a predominantly effusive eruption (Thorarinsson and Sigvaldason, 1962). In 1875, a Plinian eruption evacuated ~0.3 km^3 of rhyolite magma, forming the Öskjuvatn caldera (Carey et al., 2010). This dual behaviour underpins an ongoing debate regarding the role of mafic versus silicic magma in the current unrest, and thus whether future activity is more likely to be effusive or explosive, with direct implications for hazard assessment.

From 1983 until mid-2021, Askja's main caldera underwent persistent subsidence. Levelling, GNSS, and InSAR show a smooth, radially symmetric bowl centred on the caldera, with rates that decay approximately exponentially through time (Pagli et al., 2006; Sturkell et al., 2006). Between 2000 and 2009, InSAR time series and modelling of a deflating point source suggest a subsidence rate of ~2.2 cm yr^{-1} at 3.2-3.8 km depth with a volume decrease of 1.2×10^{-3}-1.7×10^{-3} km^3 yr^{-1} (de Zeeuw-van Dalfsen et al., 2012). Microgravity campaigns between 1988 and 2017 reveal a net gravity decrease coincident with the subsidence, consistent with mass loss and/or density reduction in a shallow reservoir, but also show shorter-term gravity increases (e.g. 2007-2009) without changes in the long-term subsidence trend (de Zeeuw-van Dalfsen et al., 2005; Koymans et al., 2023). These results have been interpreted as cooling and contraction of a shallow magma body at ~3 km depth, possibly combined with magma withdrawal (de Zeeuw-van Dalfsen et al., 2013; Koymans et al., 2023; Parks et al., 2024).

At the end of July 2021, the deformation pattern reversed. Geodetic data show inflation centred beneath the northwestern edge of Öskjuvatn, recording ~65 cm of uplift as of September 2023, best explained by a sill-like source at 2.5-3 km depth beneath the caldera (Parks et al., 2024). Microgravity measurements suggest that the pre-inflation period between 2016-2021 was potentially associated with mass accumulation beneath the caldera, whereas the 2021 inflation episode is associated with a decrease in subsurface density and may be interpreted as vesiculation of previously emplaced magma, or replacement of dense basaltic magma with less dense rhyolite (Koymans et al., 2023). Our modelling results can be used to further interrogate the plausibility of basaltic and rhyolitic magma cooling and vesiculation in driving the unrest at Askja.

Basaltic sill simulations for Askja-like conditions are consistent with the main features of the long-term subsidence, if we consider a sill volume on the order of ~0.5-1 km^3, intermediate between our small and large endmember geometries (Fig. 5a,e). Cooling and crystallisation of such a sill would produce uplift-subsidence cycles on decadal timescales, with $|dV/dt|$ on the order of 10^{-3}

km^3 yr^{-1} that decays with time, similar to what has been inferred from geodetic data. In the relatively dry Askja basalt runs, second boiling develops late in the cooling history and generates at most a few MPa overpressure at low melt fractions, so the transition from net contraction to re-pressurisation is gradual. Although, basalt crystallisation can plausibly contribute to the observed decades-long subsidence and associated gravity change, the switch to re-pressurisation and associated uplift occur much more gradually compared to the rapid onset of inflation that has been observed at Askja since 2021.

In contrast, our hydrous Askja rhyolite simulations produce monotonous pressurisation and uplift in response to second boiling, making the observed decades of subsidence difficult to reconcile with silicic magma crystallisation. Efficient gas loss from such a shallow rhyolite sill as a source of deflation is also unlikely because the permeability of the surrounding rocks tends to decrease strongly at magmatic temperatures due to thermal crack closure and alteration-induced sealing (Gaunt et al., 2016; Heap et al., 2019). Our results show that second boiling of a previously intruded rhyolite sill would be consistent with a renewed episode of uplift. However, the rates of volume change predicted by our small sill model (20 m opening) are 1-2 orders of magnitude lower to the observed $|dV/dt|$, which averages to 0.018 km^3 yr^{-1} for the July 2021-September 2023 observation interval. Hence, a much smaller volume than considered in our simulations would be required to be consistent with the observed rates if driven solely by second boiling without injection. Taken together, our results are consistent with basaltic magma cooling driving long-term subsidence at Askja. Second boiling in a small volume rhyolite sill ($<<0.14$ km^3) is a plausible scenario to explain the recent uplift episode but does not rule out magma injection of either composition as an additional or alternative driver.

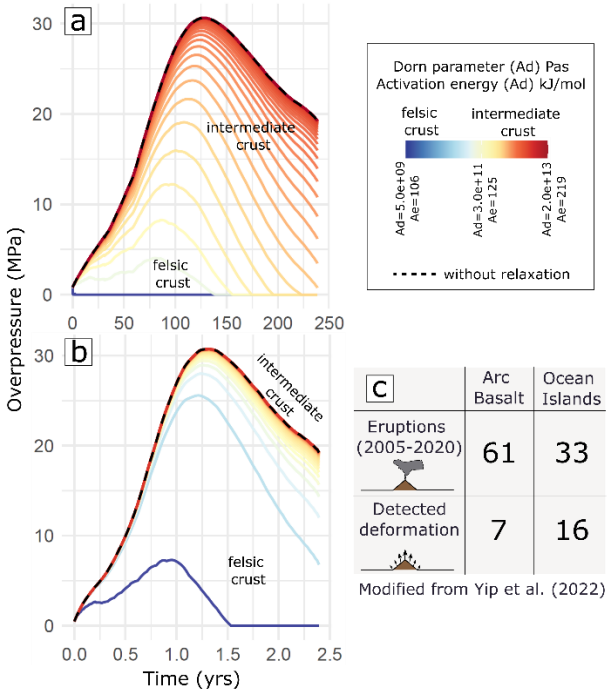

Fig. 7. *Viscoelastic relaxation of overpressure for intermediate and felsic crustal rheologies. While the intermediate crustal parameters lead to nearly elastic behaviour, felsic crust shows very efficient relaxation of overpressures. Colour coding reflects the combination of Ad and Ae used for pressure relaxation calculations. a) Large sill geometry, and b) small sill geometry. c) Global statistics of arc and ocean island basalt eruptions, modified from Yip et al. (2022).*

4.3. Crustal controls on volcano deformation

Our modelling result that sill overpressures relax efficiently only in felsic host rocks, whereas of more mafic crustal rock compositions behave quasi-elastically over cooling timescales is consistent with deformation modelling at Taal volcano (Phillipines), where only felsic crustal parameters (low activation energy - Ae and Dorn parameter - Ad) produce measurable relaxation (Morales Rivera et al., 2019). Compositional flow-law compilations further show that mafic lower-crustal rocks are characterised by even higher Ae and Ad than our intermediate case, implying even larger viscosities and less efficient relaxation at a given temperature (Kirby and Kronenberg, 1987; Ranalli and Murphy, 1987).

These rheological controls have implications for the detectability of volcanic deformation and the slow generation of overpressure. A key question is whether viscoelastic relaxation necessarily produces more or less surface deformation than a purely elastic response. Head et al. (2019, 2021) show that viscoelastic surface deformation can be either lower or higher than the elastic case depending on (i) the used rheological model (e.g., Maxwell, Standard Linear Solid, Kelvin-

Voigt) and (ii) the forcing mechanism (applied overpressure, ΔP, which imposes a stress on the source boundary, versus a volume change, ΔV, which prescribes a strain). In most cases, strain-based forcing (volume-change) tends to yield smaller surface displacements than the equivalent elastic response, while the ΔP mechanism yields larger surface displacements. Although these mechanisms are idealised endmembers, a volume-change mechanism is more consistent with our second-boiling scenario, in which volumetric expansion is the primary forcing and pressure change arises as a consequence. By contrast, the constant-stress (ΔP) endmember is more representative of a hydraulically open system where pressure is prescribed by magma influx and volume adjusts accordingly.

In crustal settings dominated by felsic, quartz-rich and/or hydrothermally altered rocks, efficient viscous relaxation around intrusions undergoing second-boiling driven volumetric expansion (ΔV) is therefore expected to reduce the amplitude of surface displacements, whereas more mafic crust should tend to maintain overpressure and respond more elastically. This provides a complementary explanation for the global pattern identified by Yip et al. (2022), who found that during the satellite era (2005-2020) deformation was detected at 48% of basaltic eruptions (16 out of 33) in ocean islands, but at only 11% of basaltic eruptions in arcs (7 out of 61) (Fig. 7c). Yip et al. (2022), attribute this contrast primarily to differences in magma compressibility during magma ascent, with hydrous arc magmas accommodating pressure changes more readily than relatively dry ocean-island basalts and thereby producing muted or absent deformation. Our results suggest that variation in host-rock rheology can already effectively mute deformation during the pressurisation stage during magma storage. More felsic upper crust typical of many arcs will favour rapid viscoelastic relaxation and thus suppress deformation signals, whereas the predominantly mafic crust beneath ocean-island volcanoes should be more elastically responsive.

Taken together, our models highlight that crustal composition exerts a first-order control on overpressure relaxation and the expression of surface deformation, consistent with earlier volcano-deformation studies (Morales Rivera et al., 2019; Rucker et al., 2022; Weber et al., 2025) and grounded in laboratory creep laws for different lithologies (Kirby and Kronenberg, 1987; Ranalli and Murphy, 1987). However, these flow laws are derived under restricted stress, temperature and timescale conditions, and our implementation necessarily simplifies the non-linear, transient and polyphase nature of crustal deformation. Dorn parameters and activation energies can have strong trade-offs and are only loosely constrained by geodetic data. Better constraints on spatially variable crustal rheology, combining laboratory experiments, petrological information and inversions of long deformation time series are therefore an important target for further research.

5. Conclusions

Our results lead to the following main conclusions:

1. Volatile-rich magmas respond very differently to cooling than relatively dry basalts. In hydrous systems and mafic-intermediate crust, second boiling rapidly drives the sill towards overpressures of a few tens of megapascals, whereas dry basaltic intrusions undergo cyclic behaviour with initial pronounced underpressure and development of modest overpressure late in their evolution.
2. The geodetic visibility of second boiling is primarily controlled by reservoir size rather than the absolute overpressure attained. For a given magma type and depth, thin and thick sills reach comparable peak overpressures, but only small, volatile-rich intrusions change volume quickly enough to generate volume change rates that exceed typical InSAR and GNSS detection thresholds.
3. The rheology of the upper crust exerts a strong influence on how overpressure is expressed at the surface. Heating of felsic, quartz-rich or altered crust produces low effective viscosities and short relaxation times, allowing overpressure to be efficiently dissipated. This is consistent with geodetic observations that arc volcanoes deform less frequently before eruptions compared to Ocean Island settings.
4. At Askja, the contrasting deformation patterns can be reconciled with a bimodal magmatic system. The long-lived subsidence phase is consistent with cooling and contraction of a shallow basaltic sill, while the rapid uplift starting in 2021 is better explained by renewed magma intrusion or vesiculation of a much smaller rhyolitic body.
5. Taken together, these findings define a regime of stealth pressurisation in shallow hydrous magma reservoirs, in which substantial overpressure can develop with little to no detectable deformation, providing a physical grounding for explosive eruptions with little precursory unrest.

Acknowledgements

We acknowledge funding to carry out this project by the European Union (ERC, MAST, Grant agreement ID: 101003173, J.B.), and by the NERC-BGS Centre for the Observation and Modeling of Earthquakes Volcanoes and Tectonics (COMET). CA acknowledges funding through a GAČR grant 23-05577S. Mike Cassidy and Steve Sparks are thanked for discussion of various aspects of this work.

Data statement

All results presented in this study have been generated using computational models. The codes to reproduce these are available in the supplementary materials to this article.

References

Albino, F., Biggs, J., Lazecký, M., Maghsoudi, Y., 2022. Routine Processing and Automatic Detection of Volcanic Ground Deformation Using Sentinel-1 InSAR Data: Insights from African Volcanoes. Remote Sensing 14, 5703. https://doi.org/10.3390/rs14225703

Annen, C., 2009. From plutons to magma chambers: Thermal constraints on the accumulation of eruptible silicic magma in the upper crust. Earth and Planetary Science Letters 284, 409–416. https://doi.org/10.1016/j.epsl.2009.05.006

Annen, C., Burgisser, A., 2021. Modeling water exsolution from a growing and solidifying felsic magma body. Lithos, 9th Hutton Symposium on the Origin of Granites and Related Rocks 402–403, 105799. https://doi.org/10.1016/j.lithos.2020.105799

Arzilli, F., Morgavi, D., Petrelli, M., Polacci, M., Burton, M., Di Genova, D., Spina, L., La Spina, G., Hartley, M.E., Romero, J.E., Fellowes, J., Diaz-Alvarado, J., Perugini, D., 2019. The unexpected explosive sub-Plinian eruption of Calbuco volcano (22–23 April 2015; southern Chile): Triggering mechanism implications. Journal of Volcanology and Geothermal Research 378, 35–50. https://doi.org/10.1016/j.jvolgeores.2019.04.006

Biggs, J., Anantrasirichai, N., Albino, F., Lazecky, M., Maghsoudi, Y., 2022. Large-scale demonstration of machine learning for the detection of volcanic deformation in Sentinel-1 satellite imagery. Bull Volcanol 84, 100. https://doi.org/10.1007/s00445-022-01608-x

Blake, S., 1984. Volatile oversaturation during the evolution of silicic magma chambers as an eruption trigger. Journal of Geophysical Research: Solid Earth 89, 8237–8244. https://doi.org/10.1029/JB089iB10p08237

Boyce, J.W., Hervig, R.L., 2009. Apatite as a monitor of late-stage magmatic processes at Volcán Irazú, Costa Rica. Contrib Mineral Petrol 157, 135–145. https://doi.org/10.1007/s00410-008-0325-x

Brookfield, A., Cassidy, M., Weber, G., Popa, R.-G., Bachmann, O., Stock, M.J., 2023. Magmatic volatile content and the overpressure 'sweet spot': Implications for volcanic eruption triggering and style. Journal of Volcanology and Geothermal Research 444, 107916. https://doi.org/10.1016/j.jvolgeores.2023.107916

Cameron, C.E., Prejean, S.G., Coombs, M.L., Wallace, K.L., Power, J.A., Roman, D.C., 2018. Alaska Volcano Observatory Alert and Forecasting Timeliness: 1989–2017. Front. Earth Sci. 6. https://doi.org/10.3389/feart.2018.00086

Carey, R.J., Houghton, B.F., Thordarson, T., 2010. Tephra dispersal and eruption dynamics of wet and dry phases of the 1875 eruption of Askja Volcano, Iceland. Bull Volcanol 72, 259–278. https://doi.org/10.1007/s00445-009-0317-3

Caricchi, L., Biggs, J., Annen, C., Ebmeier, S., 2014. The influence of cooling, crystallisation and re-melting on the interpretation of geodetic signals in volcanic systems. Earth and Planetary Science Letters 388, 166–174. https://doi.org/10.1016/j.epsl.2013.12.002

Cassidy, M., Ebmeier, S.K., Helo, C., Watt, S.F.L., Caudron, C., Odell, A., Spaans, K., Kristianto, P., Triastuty, H., Gunawan, H., Castro, J.M., 2019. Explosive Eruptions With Little Warning: Experimental Petrology and Volcano Monitoring Observations From the 2014 Eruption of Kelud, Indonesia. Geochemistry, Geophysics, Geosystems 20, 4218–4247. https://doi.org/10.1029/2018GC008161

Castro, J.M., Cordonnier, B., Schipper, C.I., Tuffen, H., Baumann, T.S., Feisel, Y., 2016. Rapid laccolith intrusion driven by explosive volcanic eruption. Nat Commun 7, 13585. https://doi.org/10.1038/ncomms13585

Castro, J.M., Schipper, C.I., Mueller, S.P., Militzer, A.S., Amigo, A., Parejas, C.S., Jacob, D., 2013. Storage and eruption of near-liquidus rhyolite magma at Cordón Caulle, Chile. Bull Volcanol 75, 702. https://doi.org/10.1007/s00445-013-0702-9

Cruden, A.R., McCaffrey, K.J.W., Bunger, A.P., 2018. Geometric Scaling of Tabular Igneous Intrusions: Implications for EmplacementLaccolithemplacementand GrowthLaccolithgrowth, in: Breitkreuz, C., Rocchi, S. (Eds.), Physical Geology of Shallow

Magmatic Systems: Dykes, Sills and Laccoliths. Springer International Publishing, Cham, pp. 11–38. https://doi.org/10.1007/11157_2017_1000
de Zeeuw-van Dalfsen, E., Pedersen, R., Hooper, A., Sigmundsson, F., 2012. Subsidence of Askja caldera 2000–2009: Modelling of deformation processes at an extensional plate boundary, constrained by time series InSAR analysis. Journal of Volcanology and Geothermal Research 213–214, 72–82. https://doi.org/10.1016/j.jvolgeores.2011.11.004
de Zeeuw-van Dalfsen, E., Rymer, H., Sigmundsson, F., Sturkell, E., 2005. Net gravity decrease at Askja volcano, Iceland: constraints on processes responsible for continuous caldera deflation, 1988–2003. Journal of Volcanology and Geothermal Research 139, 227–239. https://doi.org/10.1016/j.jvolgeores.2004.08.008
de Zeeuw-van Dalfsen, E., Rymer, H., Sturkell, E., Pedersen, R., Hooper, A., Sigmundsson, F., Ófeigsson, B., 2013. Geodetic data shed light on ongoing caldera subsidence at Askja, Iceland. Bull Volcanol 75, 709. https://doi.org/10.1007/s00445-013-0709-2
Ebmeier, S.K., Andrews, B.J., Araya, M.C., Arnold, D.W.D., Biggs, J., Cooper, C., Cottrell, E., Furtney, M., Hickey, J., Jay, J., Lloyd, R., Parker, A.L., Pritchard, M.E., Robertson, E., Venzke, E., Williamson, J.L., 2018. Synthesis of global satellite observations of magmatic and volcanic deformation: implications for volcano monitoring & the lateral extent of magmatic domains. J Appl. Volcanol. 7, 2. https://doi.org/10.1186/s13617-018-0071-3
Edmonds, M., Wallace, P.J., 2017. Volatiles and Exsolved Vapor in Volcanic Systems. Elements 13, 29–34. https://doi.org/10.2113/gselements.13.1.29
Elders, W.A., Friðleifsson, G.Ó., Albertsson, A., 2014. Drilling into magma and the implications of the Iceland Deep Drilling Project (IDDP) for high-temperature geothermal systems worldwide. Geothermics, Iceland Deep Drilling Project:The first well, IDDP-1, drilled into Magma 49, 111–118. https://doi.org/10.1016/j.geothermics.2013.05.001
Gaunt, H.E., Sammonds, P.R., Meredith, P.G., Chadderton, A., 2016. Effect of temperature on the permeability of lava dome rocks from the 2004–2008 eruption of Mount St. Helens. Bull Volcanol 78, 30. https://doi.org/10.1007/s00445-016-1024-5
Gottsmann, J., Komorowski, J.-C., Barclay, J., 2017. Volcanic Unrest and Pre-eruptive Processes: A Hazard and Risk Perspective, in: Gottsmann, Joachim, Neuberg, J., Scheu, B. (Eds.), Volcanic Unrest : From Science to Society. Springer International Publishing, Cham, pp. 1–21. https://doi.org/10.1007/11157_2017_19
Gualda, G.A.R., Ghiorso, M.S., Lemons, R.V., Carley, T.L., 2012. Rhyolite-MELTS: a Modified Calibration of MELTS Optimized for Silica-rich, Fluid-bearing Magmatic Systems. J Petrology 53, 875–890. https://doi.org/10.1093/petrology/egr080
Hauri, E.H., Maclennan, J., McKenzie, D., Gronvold, K., Oskarsson, N., Shimizu, N., 2017. CO2 content beneath northern Iceland and the variability of mantle carbon. Geology 46, 55–58. https://doi.org/10.1130/G39413.1
Head, M., Hickey, J., Gottsmann, J., Fournier, N., 2021. Exploring the Impact of Thermally Controlled Crustal Viscosity on Volcanic Ground Deformation. Journal of Geophysical Research: Solid Earth 126, e2020JB020724. https://doi.org/10.1029/2020JB020724
Head, M., Hickey, J., Gottsmann, J., Fournier, N., 2019. The Influence of Viscoelastic Crustal Rheologies on Volcanic Ground Deformation: Insights From Models of Pressure and Volume Change. Journal of Geophysical Research: Solid Earth 124, 8127–8146. https://doi.org/10.1029/2019JB017832
Heap, M.J., Troll, V.R., Kushnir, A.R.L., Gilg, H.A., Collinson, A.S.D., Deegan, F.M., Darmawan, H., Seraphine, N., Neuberg, J., Walter, T.R., 2019. Hydrothermal alteration of andesitic lava domes can lead to explosive volcanic behaviour. Nat Commun 10, 5063. https://doi.org/10.1038/s41467-019-13102-8
Humphreys, M.C.S., Smith, V.C., Coumans, J.P., Riker, J.M., Stock, M.J., de Hoog, J.C.M., Brooker, R.A., 2021. Rapid pre-eruptive mush reorganisation and atmospheric volatile emissions from the 12.9 ka Laacher See eruption, determined using apatite. Earth and Planetary Science Letters 576, 117198. https://doi.org/10.1016/j.epsl.2021.117198

Iezzi, A.M., Fee, D., Haney, M.M., Lyons, J.J., 2020. Seismo-Acoustic Characterization of Mount Cleveland Volcano Explosions. Front. Earth Sci. 8. https://doi.org/10.3389/feart.2020.573368

Kent, A.J.R., Till, C.B., Cooper, K.M., 2023. Start me up: The relationship between volcanic eruption characteristics and eruption initiation mechanisms. Volcanica 6, 161–172. https://doi.org/10.30909/vol.06.02.161172

Kilbride, B.M., Edmonds, M., Biggs, J., 2016. Observing eruptions of gas-rich compressible magmas from space. Nat Commun 7, 13744. https://doi.org/10.1038/ncomms13744

Kirby, S.H., Kronenberg, A.K., 1987. Rheology of the lithosphere: Selected topics. Reviews of Geophysics 25, 1219–1244. https://doi.org/10.1029/RG025i006p01219

Koymans, M.R., de Zeeuw-van Dalfsen, E., Sepúlveda, J., Evers, L.G., Giniaux, J.M., Grapenthin, R., Hooper, A., Ófeigsson, B.G., Sigmundsson, F., Yang, Y., 2023. Decades of subsidence followed by rapid uplift: Insights from microgravity data at Askja Volcano, Iceland. Journal of Volcanology and Geothermal Research 442, 107890. https://doi.org/10.1016/j.jvolgeores.2023.107890

Kuritani, T., Yokoyama, T., Kitagawa, H., Kobayashi, K., Nakamura, E., 2011. Geochemical evolution of historical lavas from Askja Volcano, Iceland: Implications for mechanisms and timescales of magmatic differentiation. Geochimica et Cosmochimica Acta 75, 570–587. https://doi.org/10.1016/j.gca.2010.10.009

Li, W., Costa, F., Nagashima, K., 2021. Apatite Crystals Reveal Melt Volatile Budgets and Magma Storage Depths at Merapi Volcano, Indonesia. J Petrology 62, egaa100. https://doi.org/10.1093/petrology/egaa100

Li, Y., Gregg, P.M., Lu, Z., Wang, J., 2025. Stealthy magma system behavior at Veniaminof Volcano, Alaska. Front. Earth Sci. 13. https://doi.org/10.3389/feart.2025.1535083

Mattsson, T., Burchardt, S., Almqvist, B.S.G., Ronchin, E., 2018. Syn-Emplacement Fracturing in the Sandfell Laccolith, Eastern Iceland—Implications for Rhyolite Intrusion Growth and Volcanic Hazards. Front. Earth Sci. 6. https://doi.org/10.3389/feart.2018.00005

Mbia, P.K., 2014. Sub-surface geology, petrology and hydrothermal alteration of Menengai geothermal field, Kenya. United Nations University, Reykjavík.

Morales Rivera, A.M., Amelung, F., Albino, F., Gregg, P.M., 2019. Impact of Crustal Rheology on Temperature-Dependent Viscoelastic Models of Volcano Deformation: Application to Taal Volcano, Philippines. Journal of Geophysical Research: Solid Earth 124, 978–994. https://doi.org/10.1029/2018JB016054

Namur, O., Montalbano, S., Bolle, O., Vander Auwera, J., 2020. Petrology of the April 2015 Eruption of Calbuco Volcano, Southern Chile. J Petrology 61, egaa084. https://doi.org/10.1093/petrology/egaa084

Pagli, C., Sigmundsson, F., Árnadóttir, T., Einarsson, P., Sturkell, E., 2006. Deflation of the Askja volcanic system: Constraints on the deformation source from combined inversion of satellite radar interferograms and GPS measurements. Journal of Volcanology and Geothermal Research 152, 97–108. https://doi.org/10.1016/j.jvolgeores.2005.09.014

Parks, M.M., Sigmundsson, F., Drouin, V., Hreinsdóttir, S., Hooper, A., Yang, Y., Ófeigsson, B.G., Sturkell, E., Hjartardóttir, Á.R., Grapenthin, R., Geirsson, H., Trasatti, E., Barsotti, S., Pedersen, R., Einarsson, P., Óladóttir, B.A., Friðriksdóttir, H.M., 2024. 2021–2023 Unrest and Geodetic Observations at Askja Volcano, Iceland. Geophysical Research Letters 51, e2023GL106730. https://doi.org/10.1029/2023GL106730

Poland, M.P., Anderson, K.R., 2020. Partly Cloudy With a Chance of Lava Flows: Forecasting Volcanic Eruptions in the Twenty-First Century. Journal of Geophysical Research: Solid Earth 125, e2018JB016974. https://doi.org/10.1029/2018JB016974

Popa, R.-G., Tollan, P., Bachmann, O., Schenker, V., Ellis, B., Allaz, J.M., 2021. Water exsolution in the magma chamber favors effusive eruptions: Application of Cl-F partitioning behavior at the Nisyros-Yali volcanic area. Chemical Geology 570, 120170. https://doi.org/10.1016/j.chemgeo.2021.120170

Ranalli, G., Murphy, D.C., 1987. Rheological stratification of the lithosphere. Tectonophysics 132, 281–295. https://doi.org/10.1016/0040-1951(87)90348-9
Rivalta, E., Segall, P., 2008. Magma compressibility and the missing source for some dike intrusions. Geophysical Research Letters 35. https://doi.org/10.1029/2007GL032521
Rooyakkers, S.M., Stix, J., Berlo, K., Petrelli, M., Sigmundsson, F., 2021. Eruption risks from covert silicic magma bodies. Geology 49, 921–925. https://doi.org/10.1130/G48697.1
Rucker, C., Erickson, B.A., Karlstrom, L., Lee, B., Gopalakrishnan, J., 2022. A Computational Framework for Time-Dependent Deformation in Viscoelastic Magmatic Systems. Journal of Geophysical Research: Solid Earth 127, e2022JB024506. https://doi.org/10.1029/2022JB024506
Schattel, N., Portnyagin, M., Golowin, R., Hoernle, K., Bindeman, I., 2014. Contrasting conditions of rift and off-rift silicic magma origin on Iceland. Geophysical Research Letters 41, 5813–5820. https://doi.org/10.1002/2014GL060780
Schipper, C.I., Castro, J.M., Tuffen, H., Wadsworth, F.B., Chappell, D., Pantoja, A.E., Simpson, M.P., Le Ru, E.C., 2015. Cristobalite in the 2011–2012 Cordón Caulle eruption (Chile). Bull Volcanol 77, 34. https://doi.org/10.1007/s00445-015-0925-z
Scholz, K., Townsend, M., Huber, C., Troch, J., Bachmann, O., Coonin, A.N., 2023. Investigating the Impact of an Exsolved H2O-CO2 Phase on Magma Chamber Growth and Longevity: A Thermomechanical Model. Geochemistry, Geophysics, Geosystems 24, e2023GC011151. https://doi.org/10.1029/2023GC011151
Shishkina, T.A., Botcharnikov, R.E., Holtz, F., Almeev, R.R., Portnyagin, M.V., 2010. Solubility of H2O- and CO2-bearing fluids in tholeiitic basalts at pressures up to 500 MPa. Chemical Geology 277, 115–125. https://doi.org/10.1016/j.chemgeo.2010.07.014
Spang, A., Burton, M., Kaus, B.J.P., Sigmundsson, F., 2022. Quantification of Volcano Deformation Caused by Volatile Accumulation and Release. Geophysical Research Letters 49, e2021GL097502. https://doi.org/10.1029/2021GL097502
Stock, M.J., Humphreys, M.C.S., Smith, V.C., Isaia, R., Pyle, D.M., 2016. Late-stage volatile saturation as a potential trigger for explosive volcanic eruptions. Nature Geosci 9, 249–254. https://doi.org/10.1038/ngeo2639
Stonadge, G., Miles, A., Smith, D., Large, S., Knott, T., 2023. The volatile record of volcanic apatite and its implications for the formation of porphyry copper deposits. Geology 51, 1158–1162. https://doi.org/10.1130/G51461.1
Sturkell, E., Sigmundsson, F., Slunga, R., 2006. 1983–2003 decaying rate of deflation at Askja caldera: Pressure decrease in an extensive magma plumbing system at a spreading plate boundary. Bull Volcanol 68, 727–735. https://doi.org/10.1007/s00445-005-0046-1
Tait, S., Jaupart, C., Vergniolle, S., 1989. Pressure, gas content and eruption periodicity of a shallow, crystallising magma chamber. Earth and Planetary Science Letters 92, 107–123. https://doi.org/10.1016/0012-821X(89)90025-3
Teplow, W., 2009. Dacite Melt at the Puna Geothermal Venture Wellfield, Big Island of Hawaii. Geotherm. Resour. Counc. Trans.
Thorarinsson, S., Sigvaldason, G.E., 1962. The eruption in Askja, 1961; a preliminary report. American Journal of Science 260, 641–651. https://doi.org/10.2475/ajs.260.9.641
Townsend, M., 2022. Linking surface deformation to thermal and mechanical magma chamber processes. Earth and Planetary Science Letters 577, 117272. https://doi.org/10.1016/j.epsl.2021.117272
Turner, S.J., Langmuir, C.H., Katz, R.F., Dungan, M.A., Escrig, S., 2016. Parental arc magma compositions dominantly controlled by mantle-wedge thermal structure. Nature Geosci 9, 772–776. https://doi.org/10.1038/ngeo2788
Utami, S.B., Costa, F., Lesage, P., Allard, P., Humaida, H., 2021. Fluid Fluxing and Accumulation Drive Decadal and Short-Lived Explosive Basaltic Andesite Eruptions Preceded by Limited Volcanic Unrest. J Petrology 62, egab086. https://doi.org/10.1093/petrology/egab086

Weber, G., Biggs, J., Annen, C., 2025. Distinct patterns of volcano deformation for hot and cold magmatic systems. Nat Commun 16, 532. https://doi.org/10.1038/s41467-024-55443-z

Weber, G., Simpson, G., Caricchi, L., 2020. Magma diversity reflects recharge regime and thermal structure of the crust. Sci Rep 10, 11867. https://doi.org/10.1038/s41598-020-68610-1

Yip, S.T.H., Biggs, J., Edmonds, M., Liggins, P., Shorttle, O., 2022. Contrasting Volcanic Deformation in Arc and Ocean Island Settings Due To Exsolution of Magmatic Water. Geochemistry, Geophysics, Geosystems 23, e2022GC010387. https://doi.org/10.1029/2022GC010387